

# Patterns of Convection in Rotating Spherical Shells

by R. Simitev and F.H. Busse

Institute of Physics, University of Bayreuth, D-95440 Bayreuth, Germany

## Abstract

New J. Phys., 5, pp. 97.1-97.20, DOI:10.1088/1367-2630/5/1/397, 2003.

Patterns of convection in internally heated, self gravitating rotating spherical fluid shells are investigated through numerical simulations. While turbulent states are of primary interest in planetary and stellar applications the present paper emphasizes more regular dynamical features at Rayleigh numbers not far above threshold which are similar to those which might be observed in laboratory or space experiments. Amplitude vacillations and spatial modulations of convection columns are common features at moderate and large Prandtl numbers. In the low Prandtl number regime equatorially attached convection evolves differently with increasing Rayleigh number and exhibits an early transition into a chaotic state. Relationships of the dynamical features to coherent structures in fully turbulent convection states are emphasized.

## 1 Introduction

Thermal convection in a rotating spherical fluid shell represents one of the fundamental systems on which a considerable part of the understanding of many observed geophysical, planetary and astrophysical phenomena is based. It is generally believed that the magnetic field exhibited by celestial bodies is generated in their interiors by convection driven by thermal and compositional buoyancy. Cloud patterns and the differential rotation seen at the surface of the major planets are likely to be connected with convection in the deep atmospheres of those planets (Busse, 1976, 1994). Considerable attention has therefore been devoted to the study of dynamical properties of rotating spherical shells. For recent reviews we refer to the papers by Zhang and Busse (1998) and Busse (2002).

Because a radially directed buoyancy force can not be easily realized in Earth-bound laboratories, experimenters had to resort to the use of centrifugal accelerations (Busse and Carrigan, 1976) or use spacecrafts for their experiments (Hart *et al.* 1986). Fortunately, it has turned out that the component of gravity perpendicular to the axis of rotation is much more important than the component parallel to it.

The centrifugal force is thus a convenient substitute since through the reversal of the applied temperature gradient the same buoyancy can be obtained as for the inward directed component of gravity perpendicular to the axis. Moreover, the centrifugal force increases with the distance from the axis just as the case of the gravity field of a spherical body of constant density. The use of electric fields (Hart *et al.* 1986) or magnetic fields with ferrofluids (Rosenzweig *et al.* 1999) leads to rather different radial dependences of the effective gravity. It must be admitted, however, that the absence of an axial component of gravity in experiments employing the centrifugal force leads to a thermal wind type flow in the basic state. But this can be minimized when the Coriolis parameter is sufficiently large or when a thin spherical shell is used as for example in the experimental realization of convection shown in figure 1.

In this paper results from a numerical study will be reported that have been obtained with essentially the same computer code as employed in earlier studies focusing on turbulent convection (Tilgner and Busse, 1997) and on the generation of magnetic fields (Grote and Busse, 2001). The mathematical formulation and the description of the numerical method given in section 2 can thus be kept brief. In section 3 a short introduction to the results of linear theory for the onset of convection will be given. In section 4 properties of columnar convection at Prandtl numbers of the order unity will be described and some animations of the time dependence will be presented. Equatorially attached convection flows are the subject of section 5. Their properties at finite amplitudes are studied here for the first time. Because of the required high numerical resolution in time as well as in space the low Prandtl number regime of fully nonlinear convection has posed a significant computational challenge until now. As will be shown the continuity of the convection heat flux requires that equatorially attached convection must be joined by columnar convection as the Rayleigh number increases significantly above its critical value. A concluding discussion will be given in section 6.

## 2 Mathematical Formulation and Numerical Method

For the description of finite amplitude convection in rotating spherical fluid shells we follow the standard formulation used by many authors Zhang and Busse(1987), Ardes *et al.* (1997), Zhang(1991, 1992). It is assumed that a general static state exists with the temperature distribution  $T_S = T_0 - \beta d^2 r^2 / 2 + \Delta T \eta r^{-1} (1 - \eta)^{-2}$  where  $\eta$  denotes the ratio of inner to outer radius of the shell and  $d$  is its thickness.  $\Delta T$  is the temperature difference between the boundaries in the special case  $\beta = 0$  of vanishing internal heat sources. The gravity field is given by  $\mathbf{g} = -\gamma d \mathbf{r}$  where  $\mathbf{r}$  is the position vector with respect to the center of the sphere and  $r$  is its length measured in units of  $d$ . In addition to the length  $d$ , the time  $d^2/\nu$  and the temperature  $\nu^2/\gamma \alpha d^4$  are used as scales for the dimensionless description of the problem where  $\nu$  denotes the kinematic viscosity of the fluid and  $\kappa$  its thermal diffusivity. The density is assumed to be constant except in the gravity term where its temperature dependence given by  $\alpha \equiv (d\rho/dT)/\rho = \text{const.}$  is taken into account. The basic

equations of motion and the heat equation for the deviation  $\Theta$  from the static temperature distribution are thus given by

$$\partial_t \mathbf{u} + \mathbf{u} \cdot \nabla \mathbf{u} + \tau \mathbf{k} \times \mathbf{u} = -\nabla \pi + \Theta \mathbf{r} + \nabla^2 \mathbf{u} \quad (1a)$$

$$\nabla \cdot \mathbf{u} = 0 \quad (1b)$$

$$P(\partial_t \Theta + \mathbf{u} \cdot \nabla \Theta) = (R_i + R_e \eta r^{-3} (1 - \eta)^{-2}) \mathbf{r} \cdot \mathbf{u} + \nabla^2 \Theta \quad (1c)$$

where the Rayleigh numbers  $R_i$  and  $R_e$ , the Coriolis parameter  $\tau$  and the Prandtl number  $P$  are defined by

$$R_i = \frac{\alpha \gamma \beta d^6}{\nu \kappa}, \quad R_e = \frac{\alpha \gamma \Delta T d^4}{\nu \kappa}, \quad \tau = \frac{2 \Omega d^2}{\nu}, \quad P = \frac{\nu}{\kappa}.$$

Since the velocity field  $\mathbf{u}$  is solenoidal the general representation in terms of poloidal and toroidal components can be used,

$$\mathbf{u} = \nabla \times (\nabla v \times \mathbf{r}) + \nabla w \times \mathbf{r}.$$

By multiplying the  $(\text{curl})^2$  and the curl of equation (1a) by  $\mathbf{r}$  we obtain two equations for  $v$  and  $w$ ,

$$[(\nabla^2 - \partial_t) L_2 + \tau \partial_\phi] \nabla^2 v + \tau Q w - L_2 \Theta = -\mathbf{r} \cdot \nabla \times [\nabla \times (\mathbf{u} \cdot \nabla \mathbf{u})] \quad (2a)$$

$$[(\nabla^2 - \partial_t) L_2 + \tau \partial_\phi] w - \tau Q v = \mathbf{r} \cdot \nabla \times (\mathbf{u} \cdot \nabla \mathbf{u}) \quad (2b)$$

where  $\partial_t$  and  $\partial_\phi$  denote the partial derivatives with respect to time  $t$  and with respect to the angle  $\phi$  of a spherical system of coordinates  $r, \theta, \phi$  and where the operators  $L_2$  and  $Q$  are defined by

$$L_2 \equiv -r^2 \nabla^2 + \partial_r (r^2 \partial_r) \quad (3a)$$

$$Q \equiv r \cos \theta \nabla^2 - (L_2 + r \partial_r) (\cos \theta \partial_r - r^{-1} \sin \theta \partial_\theta). \quad (3b)$$

Stress-free boundaries with fixed temperatures are most often assumed,

$$v = \partial_{rr}^2 v = \partial_r (w/r) = \Theta = 0 \quad (4)$$

$$\text{at } r = r_i \equiv \eta / (1 - \eta) \quad \text{and at } r = r_o = (1 - \eta)^{-1}$$

but sometimes no-slip boundaries are used in which case the conditions  $\partial_{rr}^2 v = \partial_r (w/r) = 0$  must be replaced by  $\partial_r (rv) = w = 0$ . For simplicity we shall assume the previously used value  $\eta = 0.4$  unless indicated otherwise. The numerical integration of equations (1c) and (2) together with boundary conditions (4) proceeds with the pseudo-spectral method which is based on an expansion of all dependent variables in spherical harmonics for the  $\theta, \phi$ -dependences, i.e.

$$v = \sum_{l,m} V_l^m(r, t) P_l^m(\cos \theta) \exp\{im\phi\} \quad (5)$$

and analogous expressions for the other variables,  $w$  and  $\Theta$ .  $P_l^m$  denotes the associated Legendre functions. For the  $r$ -dependence expansions in Chebychev polynomials are used. Spherical harmonics up to the order of  $l = 96$  and up to 41 collocation

points in radial direction have been used. A time step as low as  $10^{-6}$  was required for the computations of the small Prandtl number cases reported in section 5. For further details see Busse *et al.* (1998), Tilgner and Busse (1997).

Benchmark comparisons for stationary solutions of equations (1c) and (2) together with conditions (4) when the dynamo process is included have been done in the past (Christensen *et al.*, 2001).

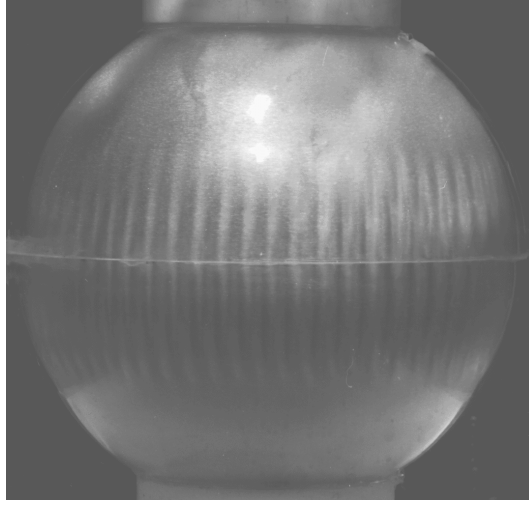


**Figure 1:** *Banana cells in a thin rotating spherical fluid shell cooled from within. The motion is made visible by a suspension of flakes which become aligned with the shear.*

### 3 Onset of Convection in Rotating Spherical Shells

A rough idea of the dependence of the critical Rayleigh number  $R_{ic}$  on the parameters of the problem in the case of internal heating can be gained from the expressions derived from the annulus model (Busse, 1970)

$$R_{ic} = 3 \left( \frac{P\tau}{1+P} \right)^{\frac{4}{3}} (\tan \theta_m)^{\frac{8}{3}} r_m^{-\frac{1}{3}} 2^{-\frac{2}{3}} \quad (6a)$$

$$m_c = \left( \frac{P\tau}{1+P} \right)^{\frac{1}{3}} (r_m \tan \theta_m)^{\frac{2}{3}} 2^{-\frac{1}{6}} \quad (6b)$$

$$\omega_c = \left( \frac{\tau^2}{(1+P)^2 P} \right)^{\frac{1}{3}} 2^{-\frac{5}{6}} (\tan^2 \theta_m / r_m)^{\frac{2}{3}} \quad (6c)$$

where  $r_m$  refers to the mean radius of the fluid shell,  $r_m = (r_i + r_o)/2$ , and  $\theta_m$  to the corresponding colatitude,  $\theta_m = \arcsin(r_m(1 - \eta))$ . The azimuthal wavenumber of the preferred mode is denoted by  $m_c$  and the corresponding angular velocity of the drift of the convection columns in the prograde direction is given by  $\omega_c/m_c$ . In figure 2 the expressions (6a, 6c) are compared with accurate numerical values

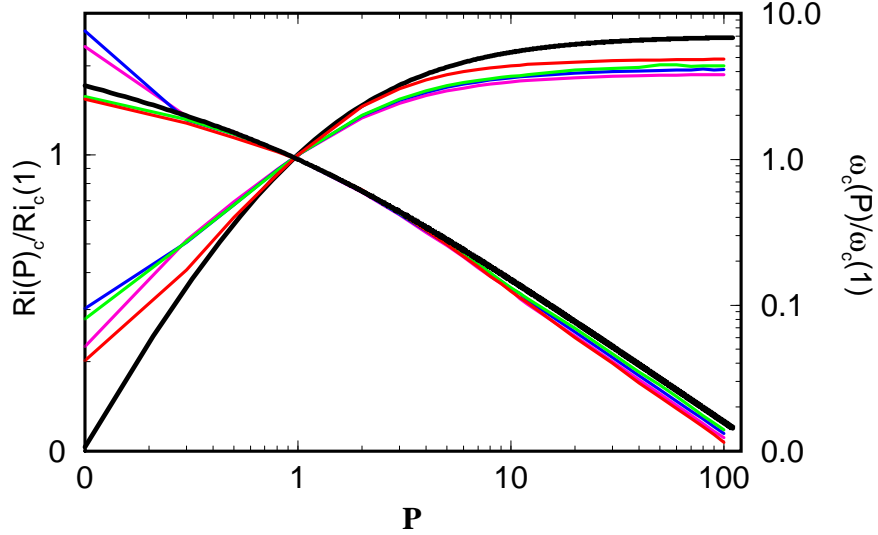


**Figure 2:** Critical Rayleigh number  $R_{ic}$  and frequency  $\omega_c$  (right ordinate) as a function of the Prandtl number  $P$  in the case  $\eta = 0.4$  for the Coriolis numbers  $\tau = 5 \cdot 10^3$  (pink),  $10^4$  (blue),  $1.5 \cdot 10^4$  (green) and  $10^5$  (red). The thick black line corresponds to expressions (6a) and (6c). The reference value  $R_{ic}(1)$  equals 80296, 190140, 318395, 3665919 for  $\tau = 5 \cdot 10^3, 10^4, 1.5 \cdot 10^4, 10^5$ , respectively. For expression (6a)  $R_{ic}(1)$  is given by  $0.67543 \cdot \tau^{4/3}$ .

which indicate that the general trend is well represented by expressions (6a, 6c). The same property holds for  $m_c$ . For a rigorous asymptotic analysis including the radial dependence we refer to Jones *et al.* (2000). In the following we shall continue to restrict the attention to the case  $R_e = 0$  and thus we shall drop the subscript  $i$  of  $R_i$ .

There is a second mode of convection which becomes preferred at onset for sufficiently low Prandtl numbers. It is characterized by convection cells attached to the equatorial part of the outer boundary not unlike the “banana cells” seen in the narrow gap experiment of figure 1. The equatorially attached mode actually represents an inertial wave modified by the effects of viscous dissipation and thermal buoyancy. An analytical description of this type of convection can thus be attained through the introduction of viscous friction and buoyancy as perturbations as has been done by Zhang (1994) for the case of stress-free as well as for no-slip boundaries (Zhang, 1995). According to Ardes *et al.* (1997) equatorially attached convection is preferred at onset for  $\tau < \tau_l$  where  $\tau_l$  increases in proportion to  $P^{1/2}$ .

In the derivation of the asymptotic relationships (6) the exact nature of the boundary condition for the tangential component of the velocity vector at the spherical surface does not enter. In the limit of infinite  $\tau$  the conditions of onset of convections are the same for no-slip and for stress-free conditions. In the following we shall restrict the attention, however, to the case of stress-free boundaries in order to avoid the complications arising from Ekman boundary layers at no-slip surfaces.

## 4 Evolution of Convection Columns at Moderate Prandtl Numbers

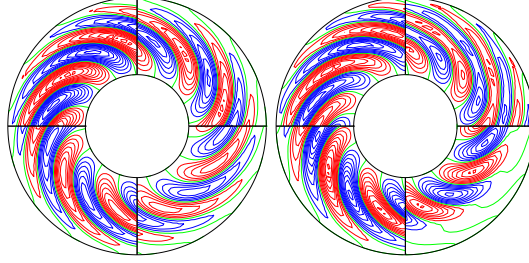


**Figure 3:** Lines of constant  $r \frac{\partial v}{\partial \phi}$  in the equatorial plane in the case  $\tau = 3 \cdot 10^4$ ,  $P = 0.1$  for  $R = 3 \cdot 10^5$  (left) and for  $R = 3.5 \cdot 10^5$  (right). The four sections are a quarter of the vacillation period,  $t_p = 0.0864$  (left) and  $t_p = 0.0124$  (right), apart with time progressing in the clockwise sense.

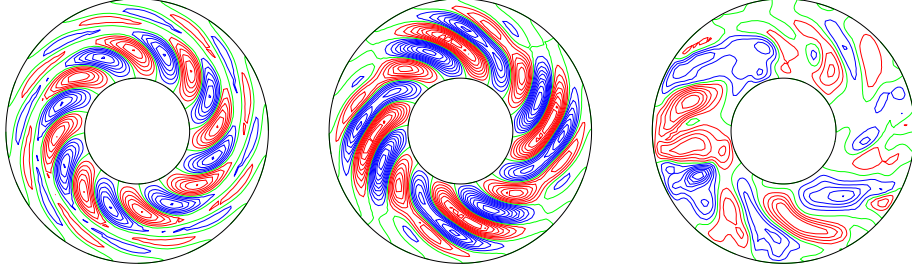
In general the onset of convection in rotating fluid spheres occurs supercritically. As long as the convection assumes the form of shape preserving travelling thermal Rossby waves as described by linear theory, its azimuthally averaged properties are time independent. In fact, as seen from a frame of reference drifting together with the convection columns the entire pattern is steady. A differential rotation is generated through the action of the Reynolds stress. The latter is caused by the spiralling cross section of the columns which persists as a dominant feature at moderate Prandtl numbers far into the turbulent regime. The plots of the streamlines  $r \frac{\partial v}{\partial \phi} = \text{const.}$  in the equatorial plane shown in figure 3 give a good impression of the spiralling nature of the columns.

A true time dependence of convection develops in the form of vacillations after a subsequent bifurcation. First the transition to amplitude vacillations occurs in which case just the amplitude of convection varies periodically in time as exhibited in the left plot of figure 3. At a somewhat higher Rayleigh number shape vacillations become noticeable which are characterized by periodic changes in the structure of the columns as shown in the right plot of figure 3. The outer part of the columns is stretched out, breaks off and decays. The thinning and subsequent breakup can actually be best seen in movie 1. The tendency towards breakup is caused by the fact that the local frequency of propagation varies with distance from the axis according to expression (6c) after  $\theta_m$  has been replaced by the local colatitude  $\theta$ .

The two types of vacillations also differ significantly in their frequencies of oscillation. This is evident from the time records of the energy densities of convection which have been plotted in figure 4. The various components of the energy densities are defined by

$$E_p^m = \frac{1}{2} \langle |\nabla \times (\nabla \bar{v} \times \mathbf{r})|^2 \rangle, \quad E_t^m = \frac{1}{2} \langle |\nabla \bar{w} \times \mathbf{r}|^2 \rangle \quad (7)$$

$$E_p^f = \frac{1}{2} \langle |\nabla \times (\nabla \check{v} \times \mathbf{r})|^2 \rangle, \quad E_t^f = \frac{1}{2} \langle |\nabla \check{w} \times \mathbf{r}|^2 \rangle \quad (8)$$



Movies 1, 2 and 3.

where  $\bar{v}$  refers to the azimuthally averaged component of  $v$  and  $\check{v}$  is given by  $\check{v} = v - \bar{v}$ .

As the Rayleigh number is increased further a fairly sudden transition into a chaotic regime occurs where convection has become strongly inhomogeneous in space and in time. A typical sequence of plots is shown in figure 5 which covers about one period of the relaxation cycles seen in the time record for  $R = 3.8 \cdot 10^5$  in figure 4. In contrast to the more common relaxation oscillations encountered at higher Rayleigh numbers, see, for example, the time record for  $R = 5 \cdot 10^5$  in figure 4, convection does not die off entirely at any time during the cycle. But the interaction between convection and differential rotation appears to be similar. As the amplitude of convection as measured by  $E_p$  and  $E_t$  grows the differential rotation generated by the Reynolds stress grows as well with just a small delay in time. When the differential rotation reaches a critical level the convection columns become disrupted and their amplitude decays. Subsequently the differential rotation decays as well on the time scale of viscous diffusion. It is typical for this type of relaxation cycles that the viscous decay is shorter than the growth time of the differential rotation in contrast to the relaxation oscillations at higher values of  $R$ . The regime of relaxation oscillations is interrupted once in a while by a return to the more regular regime of shape vacillations as shown in the inserted enlargement of the time record for  $R = 3.8 \cdot 10^5$  in figure 4. But in contrast to the vacillation of the right plot figure 3 the pattern is now strongly modulated. The component with the azimuthal wavenumber  $m=1$  plays a dominant role in this modulation. As can be seen in figure 6 the pattern recurs nearly periodically in time in spite of the modulation. Figure 6 corresponds to the slightly higher Rayleigh number of  $4 \cdot 10^5$  where convection changes intermittently between relaxation cycles and vacillation oscillations.

As  $R$  is further increased the spatio-temporal structure of convection becomes more irregular as can be seen in the time series for  $R = 4.5 \cdot 10^5$  in figure 4. But at  $R = 5 \cdot 10^5$  the relaxation oscillations with only intermittent convection become firmly established and they continue to persist up to Rayleigh numbers of the order of  $1 \cdot 10^6$ . They are basically the same phenomenon as found by Grote and Busse (2001) at  $P = 1$  and even the period is the same, about 0.1, which corresponds to the viscous decay time of the differential rotation. The only difference that can be noted is the small precursor hump before the burst of convection. In figure 7

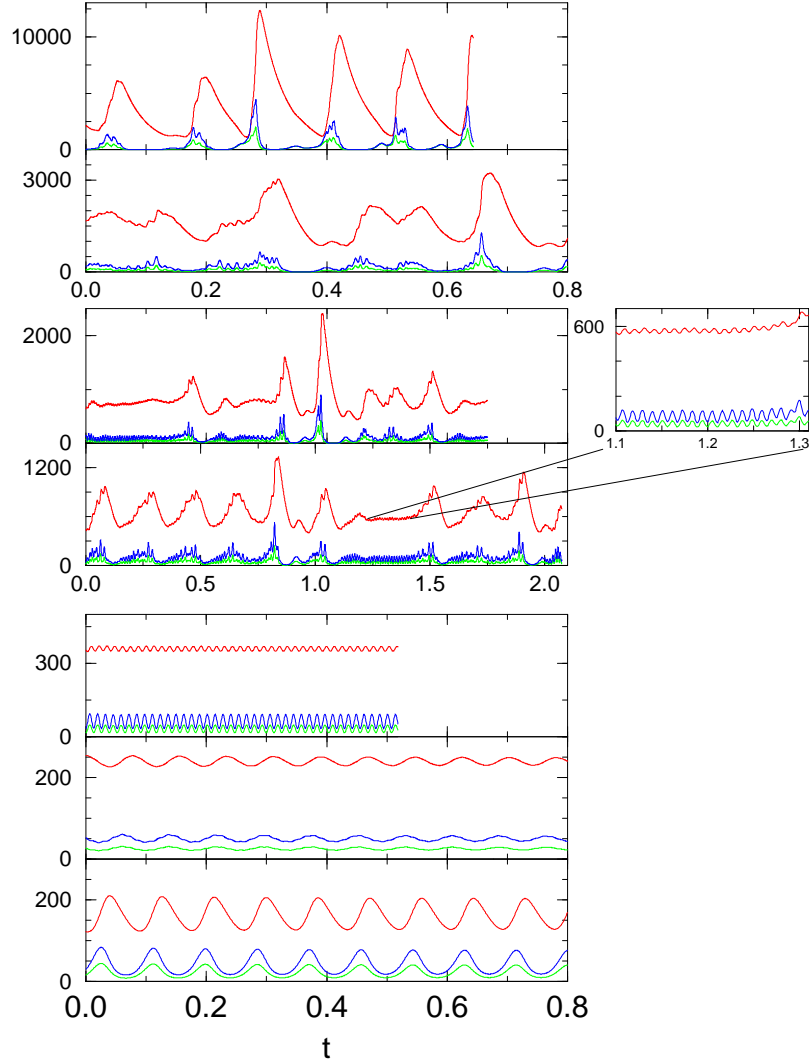


**Figure 4:** Time series of energy densities of convection in the case  $\tau = 3 \cdot 10^4$ ,  $P = 0.1$  for  $R = 3 \cdot 10^5$ ,  $3.3 \cdot 10^5$ ,  $3.5 \cdot 10^5$ ,  $3.8 \cdot 10^5$ ,  $4 \cdot 10^5$ ,  $4.5 \cdot 10^5$ ,  $5 \cdot 10^5$  (from bottom to top). Red, blue and green lines indicate  $E_t^m$ ,  $E_t^f$ , and  $E_p^f$  respectively. The critical Rayleigh number for onset of convection is  $R_c = 222518$ .  $E_p^m$  is smaller by more than an order of magnitude than the other energy densities and has not been plotted for this reason.

the third plot shows convection appearing in a fairly regular pattern. Afterwards it decays again as shown in the fourth plot before it erupts in a chaotic fashion as the differential rotation has reached its minimum amplitude. Since this latter part of the cycle occurs on a rather short time scale, smaller intervals between the plots have been used for this part in figure 7.

The main difference between convection at  $P = 0.1$  and Prandtl numbers of the order unity occurs at the transition between regular and irregular patterns. A typical scenario is shown in figure 8. After convection has set in in the form of eight drifting column pairs the usual amplitude vacillations occur as the Rayleigh number is increased. The shape vacillations, however, exhibit a modulation with



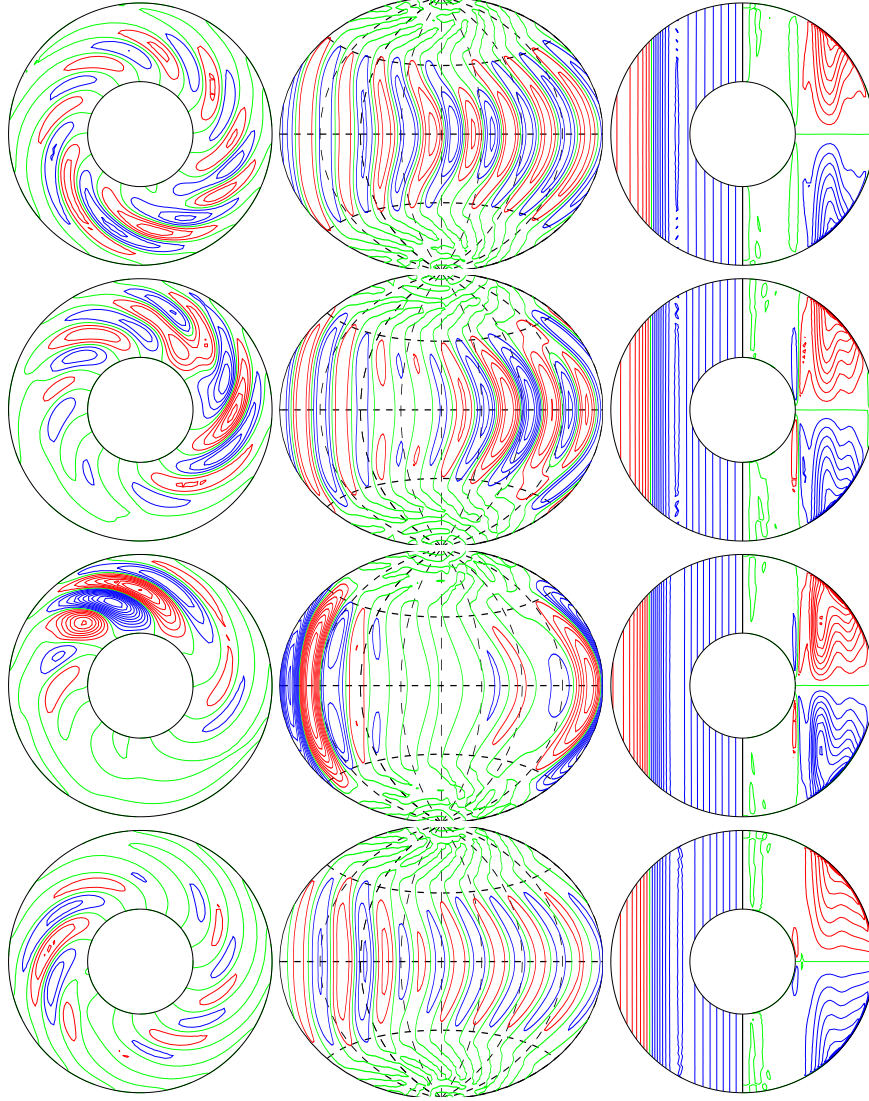


**Figure 5:** Sequence of plots equidistant in time (from top to bottom with  $\Delta t = 0.05$ ) for  $R = 3.8 \cdot 10^5$ ,  $\tau = 3 \cdot 10^4$ ,  $P = 0.1$ . The left column shows streamlines,  $r \frac{\partial v}{\partial \phi} = \text{const.}$ , in the equatorial plane and in the middle column lines of constant radial velocity  $u_r$  on the mid surface,  $r = r_i + 0.5$ , are shown. The left halves of the circles of the right column show lines of constant  $u_\phi$  which is the azimuthally averaged azimuthal component of the velocity field. The right halves show streamlines of the axisymmetric meridional circulation.

wavenumber  $m = 4$  as shown in figure 9. Only every second pair of columns gets stretched until the outer part separates, a little earlier for the cyclonic column than for the anticyclonic one. Then the same process is repeated for the other pairs of columns such that the sequence shown in figure 9 exhibits only half a period of the oscillation. In addition, of course, the column pattern drifts in the prograde direction. Movie 2 provides a vivid impression of this type of convection.

With increasing Rayleigh number the stretching process gets out of phase and

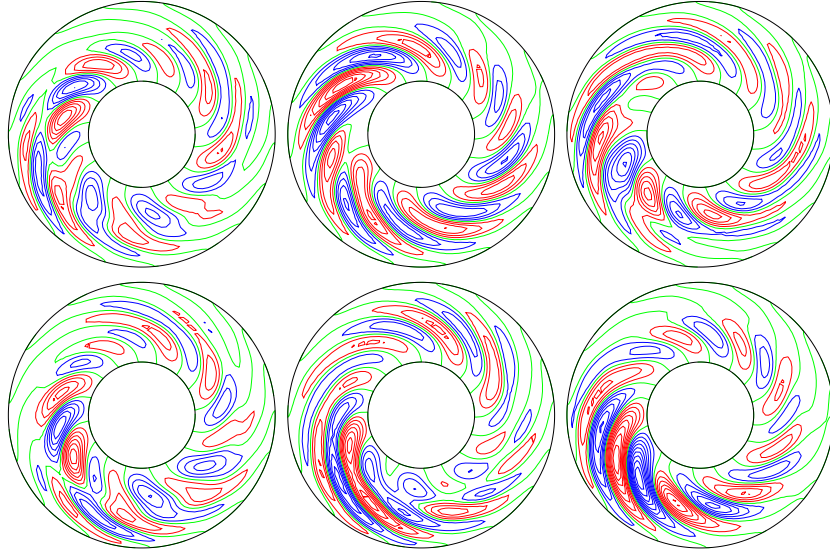


**Figure 6:** *Modulated shape vacillations of convection for  $R = 4 \cdot 10^5$ ,  $\tau = 3 \cdot 10^4$ ,  $P = 0.1$ . The sequence of plots equidistant in time ( $\Delta t = 0.00376$ ), starting at the upper left and continuing clockwise, shows streamlines,  $r \frac{dv}{d\phi} = \text{const.}$ , in the equatorial plane. Since the modulation period is  $t_p = 0.0188$ , the last plot closely resembles the first plot except for a shift in azimuth.*

an  $m = 1$ -modulation enters as shown in figure 10. The time dependence is still periodic, but has become more complex in that some of the separated outer parts become attached to the preceding column pair. To show this process in more detail some extra plots have been added to the time sequence of figure 10. While the amplitude of convection varies considerably throughout the cycle, the differential rotation exhibits only small oscillations as can be seen from the corresponding section of figure 8.

By the time when  $R$  has reached  $3.5 \cdot 10^5$  the modulated vacillations have become aperiodic and with increasing Rayleigh number convection becomes more and more chaotic. Regularity reappears only in the form relaxation oscillations as shown in the section for  $R = 7 \cdot 10^5$  of figure 8. Reminders of the vacillations can still be seen in this time record. But at  $R = 1 \cdot 10^6$  the relaxation oscillations have become fully established with convection occurring only in an intermittent fashion. Although obtained for a slightly smaller value of  $\tau$ , movie 3 gives a good impression of the onset of relaxation oscillations.

## 5 Convection at Small Prandtl Numbers

Since stellar interiors as well as metallic planetary cores are characterized by rather small Prandtl numbers much attention has been focused on the problem of the onset of convection in rotating fluid spheres in the case of small  $P$ . Zhang and Busse (1987) found the equatorially attached mode which is quite distinct from

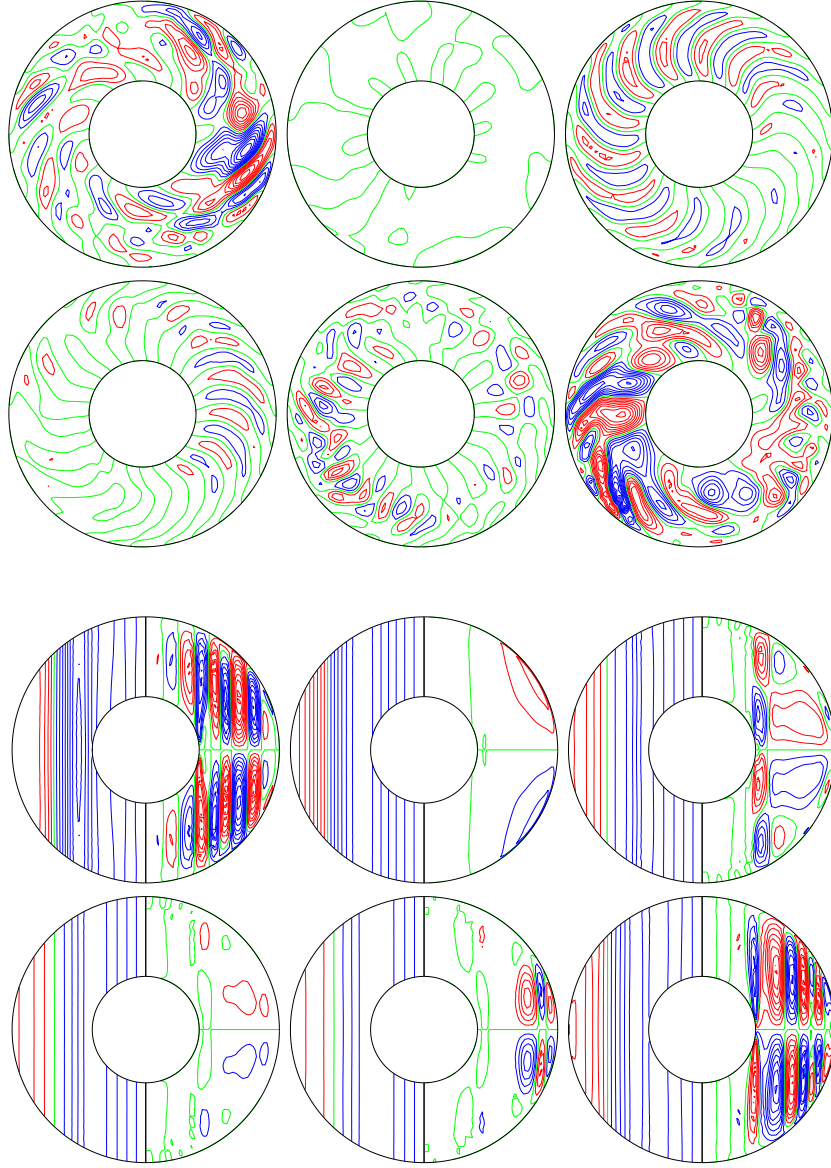


**Figure 7:** Relaxation oscillations of convection for  $R = 5 \cdot 10^5$ ,  $\tau = 3 \cdot 10^4$ ,  $P = 0.1$ . The upper 6 plots show a time sequence (upper row left to right, lower row left to right) of streamlines,  $r \frac{\partial v}{\partial \phi} = \text{const.}$ , in the equatorial plane. The corresponding lower 6 plots show lines of constant  $u_\phi$  in the left halves of the circles and the meridional circulation in the right halves. The separation in time is 0.0378 for the first four plots and 0.0126 for the last three plots.

the columnar mode discussed in the preceding section. The new mode represents an inertial oscillation which becomes excited when viscous dissipation is balanced by the energy provided by thermal buoyancy. The fact that both energies can be regarded as small perturbations has led Zhang (1994, 1995) to solve the problem of onset of convection by an asymptotic analysis. An detailed numerical study together with some analytical approximations can be found in the paper of Ardes *et al.* (1997).

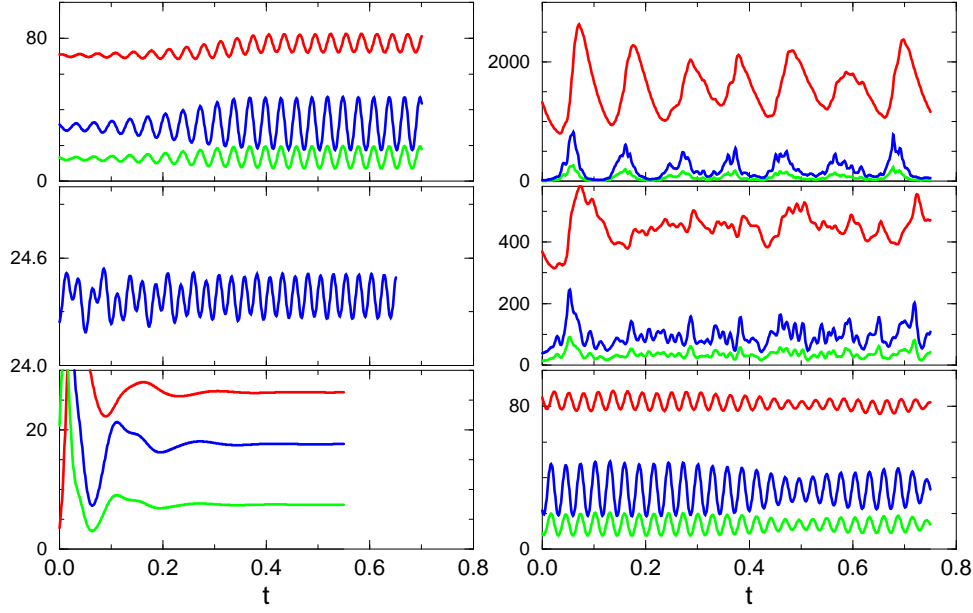


**Figure 8:** Time series of energy densities of convection in the case  $\tau = 1.5 \cdot 10^4$ ,  $P = 0.5$  for  $R = 3 \cdot 10^5$ ,  $3.2 \cdot 10^5$ ,  $3.45 \cdot 10^5$  (from bottom to top, left side) and  $R = 3.5 \cdot 10^5$ ,  $7 \cdot 10^5$ ,  $10^6$  (from bottom to top, right side). Red, blue and green lines indicate  $E_t^m$ ,  $E_t^f$ , and  $E_p^f$ , respectively. The critical Rayleigh number for onset is  $R_c = 215142$ .

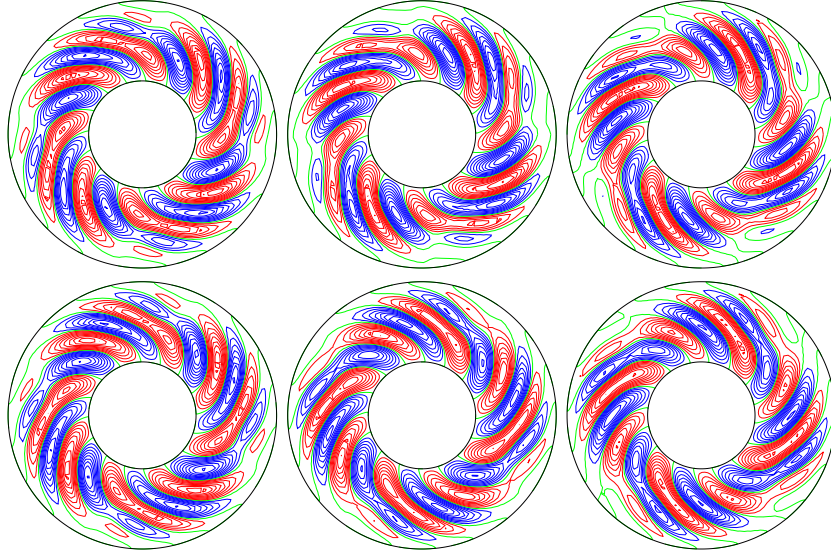


**Figure 9:** Modulated shape vacillations of convection for  $R = 3.2 \cdot 10^5$ ,  $\tau = 1.5 \cdot 10^4$ ,  $P = 0.5$ . The sequence of plots equidistant in time ( $\Delta t = 0.005$ ), starting at the upper left and continuing clockwise, shows streamlines,  $r \frac{\partial v}{\partial \phi} = \text{const.}$ , in the equatorial plane. Since the modulation period is about 0.025, the last plot resembles the first plot except for a shift in azimuth.



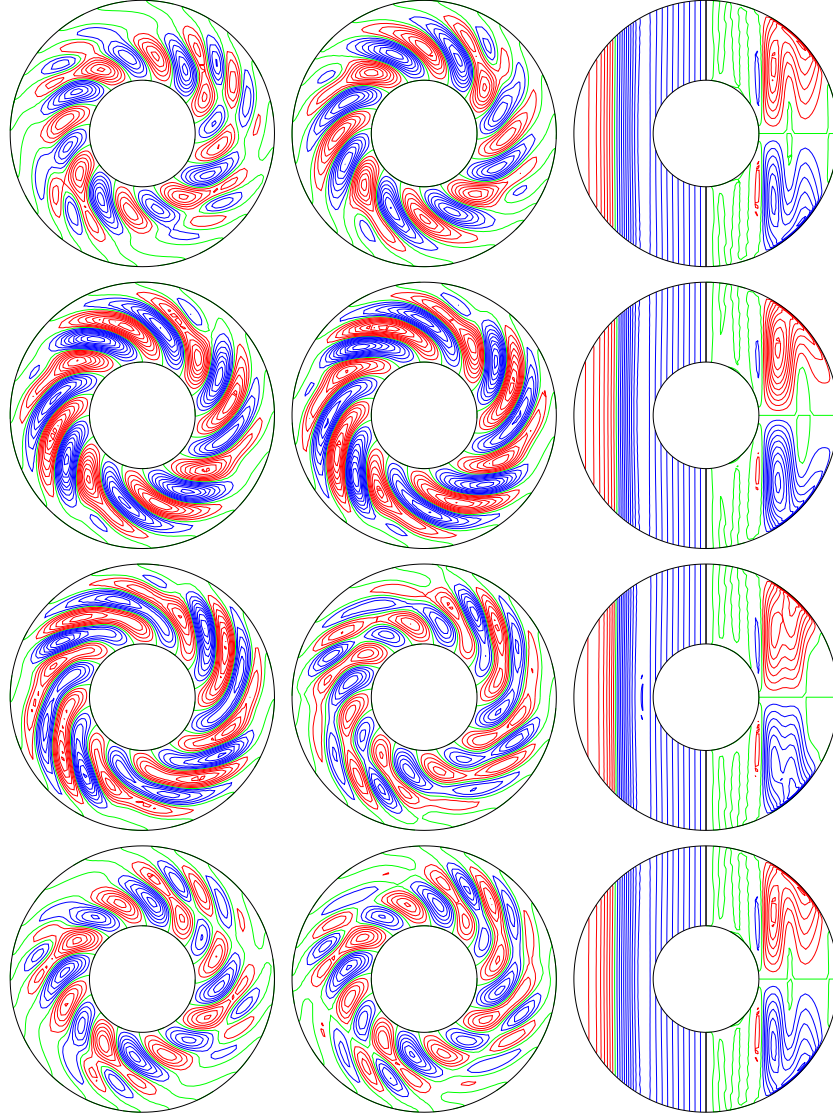


**Figure 10:** Modulated shape vacillations of convection for  $R = 3.45 \cdot 10^5$ ,  $\tau = 1.5 \cdot 10^4$ ,  $P = 0.5$ . The left and middle columns show streamlines,  $r \frac{\partial v}{\partial \phi} = \text{const.}$ , in the equatorial plane, the right column shows lines of constant  $u_\phi$  in the left halves of the circles and streamlines of the meridional circulation in the right halves. The left and the right columns show plots at the times  $t = (n-1) \cdot 0.01$ , for  $n = 1, 2, 3, 4$  (from top to bottom), the middle column shows plots at the intermediate times  $t = (n-1) \cdot 0.005$

The results of these various efforts have turned out to be rather complex since the preferred inertial modes travel in the prograde as well in the retrograde directions depending on the parameters of the problem. Moreover, the azimuthal wavenumber  $m$  of convection does not increase monotonically with the Coriolis parameter  $\tau$  as is usually found for the columnar mode at values of  $P$  of the order unity or higher. In addition to the simple "single cell" inertial modes of Zhang and Busse (1987) multicellular modes have been found in the study of Ardes *et al.* (1997)

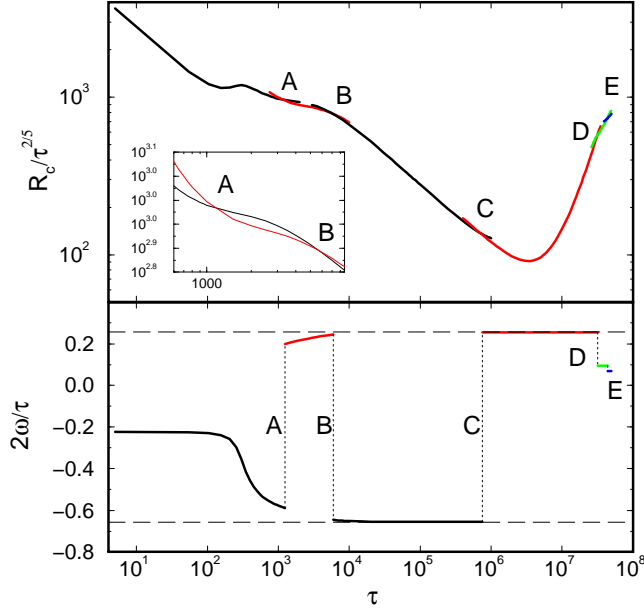


**Figure 11:** The critical Rayleigh number  $R_c$  (upper plot) and the corresponding frequency  $\omega_c$  (lower plot) as a function of  $\tau$  in the case  $P = 10^{-4}$ ,  $\eta = 0.3$ ,  $m = 8$ . The values corresponding to the analytical expression (9) for  $\omega_c$  are shown with dashed lines.

which appear to be closely related to the multicellular modes described by the Airy function in the analysis by Yano (1992) of the analogous problem of convection in the rotating cylindrical annulus. The numerical solutions for the problem obtained by Pino *et al.* (2000) also indicate the onset of multicellular convection in parts of the parameter space.

Here we shall present only some examples of the variety of patterns encountered in a rotating sphere of a low Prandtl number fluid. In figure 11 the multiple changes from retrograde to prograde modes as a function of  $\tau$  are indicated and the corresponding changes in the patterns are shown in figure 12. To facilitate comparisons the wavenumber  $m = 8$  has been kept fixed. But similar changes in the structure of convection are found when competing values of  $m$  are admitted. The retrograde and prograde modes differ little in their form. The opposite phase between toroidal and poloidal components of motion is the most characteristic difference as indicated in figure 13. The sense of outward spiralling is also opposite for prograde and retrograde modes as is evident from figure 12. But in the limit of vanishing Prandtl number the sense of spiralling disappears because the phase of the inertial modes does not vary with distance from the axis.

Whenever  $\tau$  is sufficiently large the frequency  $\omega$  is closely approximated by the frequency of the corresponding inertial modes which is given by the analytical expression (Zhang, 1994; Ardes *et al.*, 1997),

$$\omega = \frac{\tau}{m+2} (1 \pm [(1 + m(m+2)(2m+3)^{-1})^{\frac{1}{2}}]). \quad (9)$$

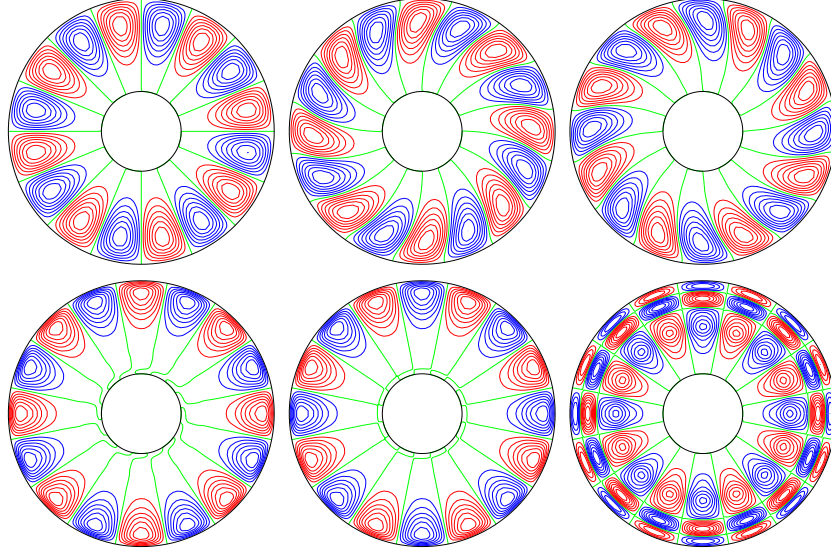


**Figure 12:** Lines of constant  $r \frac{\partial v}{\partial \phi}$  in the equatorial plane illustrating the sequence of transitions for the same parameters as Fig. 11 and values of  $\tau = 5, 950, 1500, 6 \cdot 10^5, 8 \cdot 10^5, 3.5 \cdot 10^7$  (left to right, first upper row then lower row).

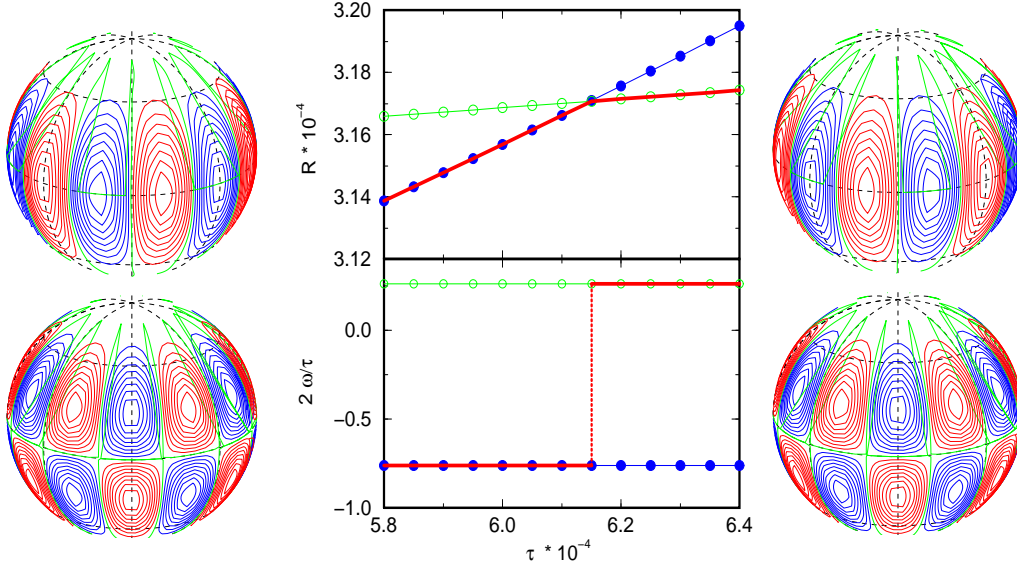


**Figure 13:** Graphs in the center show the critical Rayleigh numbers  $R_c$  of the competing prograde (green line, empty circles) and retrograde mode (blue line, filled circles) as well as the actual critical value (thick red line) and the corresponding frequencies as a function of  $\tau$  in the case  $P = 0.001, \eta = 0.2, m = 6$ . Contours of constant radial velocity  $u_r$  (lower plots) and the streamlines,  $w = \text{const.}$  on the spherical surface  $r = 0.9$  (upper plots) for  $\tau = 58000$  and  $64000$  are shown on the left and right sides, respectively.

The negative (positive) sign applies for modes drifting in the prograde (retrograde) direction. Explicit values of expression (9) are given in figures 11 and 13 for

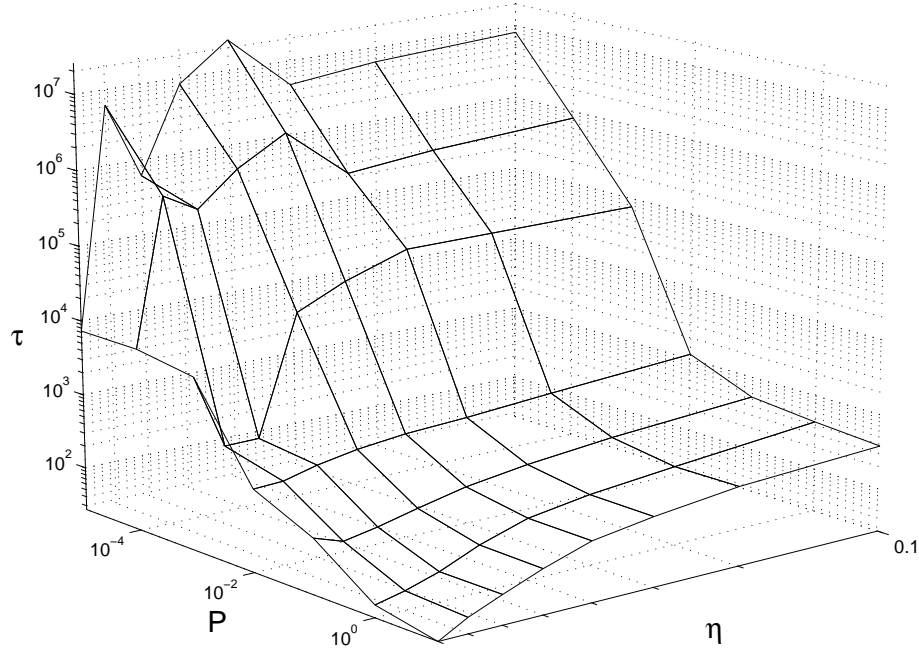


**Figure 14:** The boundary separating the retrograde (below the surface) and prograde mode (above the surface) for a fixed value of the wavenumber  $m = 6$ .

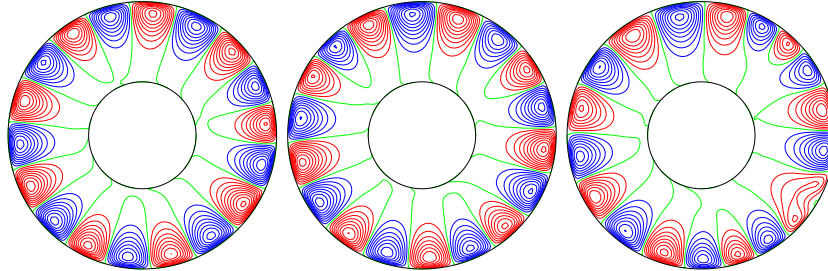


**Figure 15:** Streamlines  $r \frac{\partial v}{\partial \phi} = \text{const.}$  in the equatorial plane for the case  $P = 0.025$ ,  $\tau = 10^5$  with  $R = 3.2 \cdot 10^5$ ,  $3.4 \cdot 10^5$ ,  $3.8 \cdot 10^5$  (from left to right).

comparisons with the numerically determined values.

For an analysis of nonlinear properties of equatorially attached convection we focus on the case  $P = 0.025$  with  $\tau = 10^5$ . The critical Rayleigh number for this case is  $R_c = 28300$  corresponding to  $m = 10$ . As  $R$  is increased beyond the critical value other values of  $m$  from 7 to 12 can be realized, but  $m = 10$  and lower values are usually preferred. An asymptotic perfectly periodic solution with  $m = 10$  or  $m = 9$  can be found only for Rayleigh numbers close to the critical value when computations are started from arbitrary initial conditions. On the other hand, perfect periodic patterns appear to be stable with respect to small disturbances over a more extended regime of supercritical Rayleigh numbers. Distinct transitions like the transition to amplitude vacillations and to structure vacillations do not seem to



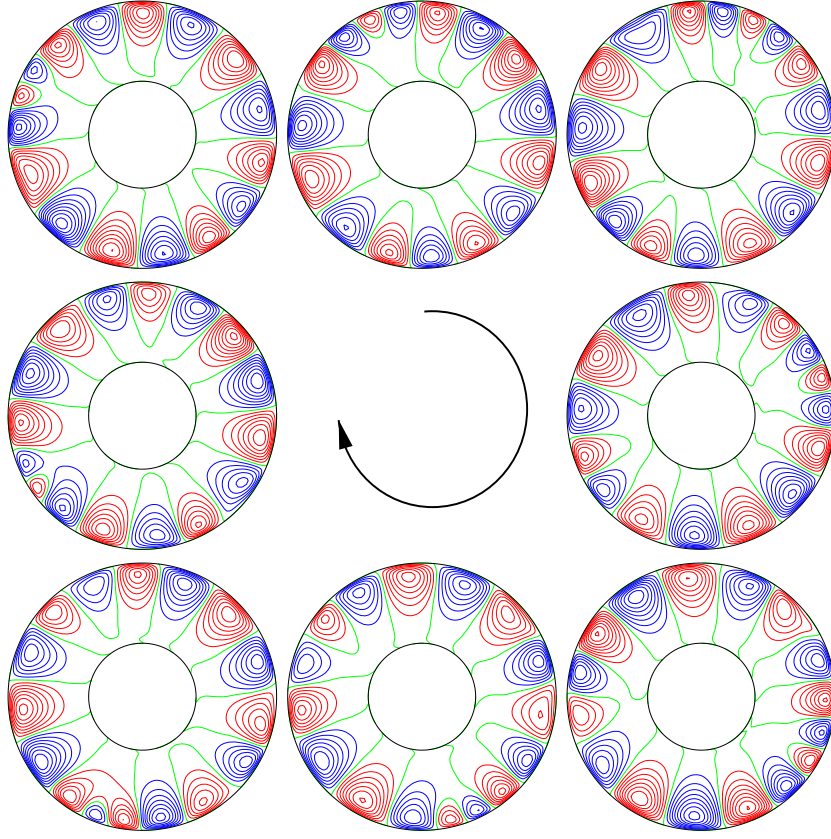


**Figure 16:** Streamlines  $r \frac{\partial v}{\partial \phi} = \text{const.}$  in the equatorial plane for the case  $P = 0.025$ ,  $\tau = 10^5$ ,  $R = 4 \cdot 10^5$ . Time increases by  $4 \cdot 10^{-3}$  from one plot to the next starting at the left upper corner. The eight plot is similar to the first one except for a shift in azimuth.

exist for equatorially attached convection. Instead modulated patterns are typically already observed when  $R$  exceeds the critical value by 10% as can be seen in the plots of figure 15. These modulations are basically caused by the interaction of two modes with neighboring values of the azimuthal wavenumber  $m$  as indicated in figure 16. Here the region of small amplitude drifts in the retrograde direction with the difference of the drift rates for  $m = 7$  and  $m = 8$ . The time series of energy densities shown in figure 17 indicate that more than two modes usually contribute to the dynamics of the pattern since the time dependence is not periodic as one would expect if only two modes interact. The computations of the time series require a high spatial resolution together with a small time step. The time spans indicated in figure 17 are sufficient for reaching a statistically steady state of the fluctuating components of motion since these equilibrate on the fast thermal time scale of the order  $P^{-1}$ . Only close to  $R_c$  the adjustment process takes longer as can be seen in the case  $R = 3.1 \cdot 10^5$  where a  $m = 10$  - pattern approaches its equilibrium state. The pattern corresponding to the other cases of figure 17 are the ones shown in figures 15, 16 and 18. The differential rotation represented by  $E_t^m$  relaxes on the viscous time scale and thus takes a long time to reach its asymptotic regime in the

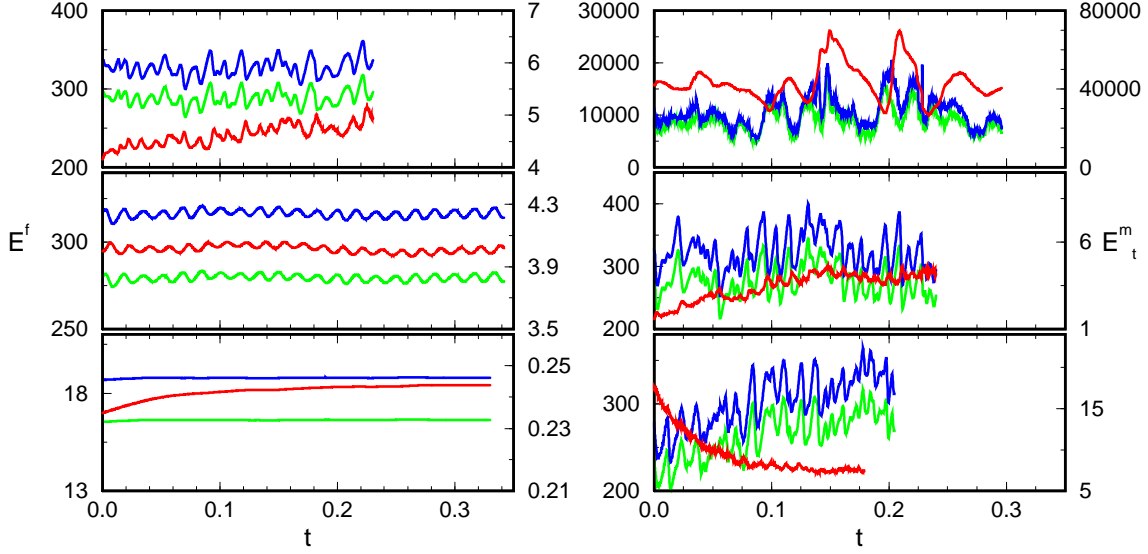


**Figure 17:** Time series of energy densities of convection in the case  $P = 0.025$ ,  $\tau = 10^5$ , for  $R = 3.1 \cdot 10^5$ ,  $3.2 \cdot 10^5$ ,  $3.4 \cdot 10^5$ , (from bottom to top, left side) and  $3.8 \cdot 10^5$ ,  $4 \cdot 10^5$ ,  $8 \cdot 10^5$  (from bottom to top, right side). The red, blue and green lines correspond to  $E_t^m$ ,  $E_t^f$ ,  $E_p^f$ , respectively.  $E_t^m$  is measured on the left ordinate.

examples shown in figure 17. But the differential rotation is quite weak such that it has a negligible effect on the other components of motion except in the case of the highest Rayleigh number of figure 17. Even smaller is the axisymmetric part of the poloidal component of motion which is not shown in the plots of figure 17. At higher Rayleigh numbers the equatorially attached eddies spread farther into the interior and in some cases become detached from the equator as can be seen in the plots of figure 18. In this way the convection eddies contribute to the heat transport from the inner boundary. But at the same time they acquire the properties of the convection columns which are characteristic for convection at higher Prandtl numbers. Accordingly the differential rotation is steeply increased at  $R = 10^6$  and a tendency towards relaxation oscillation can be noticed in the upper right time series of figure 17.

## 6 Concluding Remarks

The results on linear and nonlinear properties of low Prandtl number convection in rotating spherical shells are of special interest for applications to problems of convection in planetary and stellar interiors. Since planetary cores often consist of liquid metal or of metallic hydrogen as in the case of Jupiter and Saturn, their Prandtl numbers are rather low. Moreover, because of high temperatures radiative heat transport is no longer negligible which tends to lower the Prandtl number even more. The latter effect dominates in stellar interiors. On the other hand, turbulence owing to small scale motions which remain unresolved in numerical simulations will

tend to equalize all effective diffusivities. But this tendency is not likely to erase entirely the differences in the subgrid scale transports of heat and momentum.

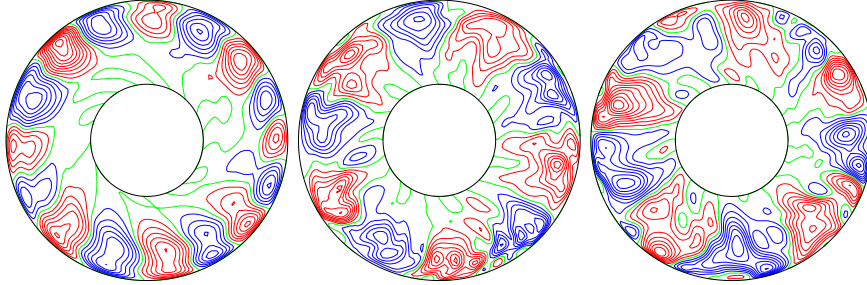


**Figure 18:** Streamlines  $r \frac{\partial v}{\partial \phi} = \text{const.}$  in the equatorial plane for the case  $P = 0.025$ ,  $\tau = 10^5$  with  $R = 6 \cdot 10^5$ ,  $8 \cdot 10^5$ ,  $10^6$  (from left to right).

Of particular interest is the effect of the Prandtl number on the dynamo action of convection. While the strong differential rotation associated with columnar convection tends to promote the generation of magnetic fields (see, for example, Grote and Busse, 2001), its near absence in the case of equatorial attached convection may increase the Rayleigh number required for dynamo action at a given value of the magnetic Prandtl number. As the Rayleigh number reaches high values more column like convection flows tend to appear near the inner boundary of the shell and are expected to promote dynamo action. Numerical studies of this problem are in progress and will be reported in the near future.

The regular and modulated patterns of convection reported in this paper as well as the coherent structures found in the chaotic regimes of convection can in principle be observed in experiments through the use of techniques mentioned in the Introduction. Low Prandtl number fluids such as liquid metals pose severe experimental challenges because convection flows can not easily be visualized. On the other hand the temperature profiles of convection patterns can be measured through time records of thermistor probes implanted in the spherical boundary since the pattern is drifting by. See, for example, measurements of convection in mercury in the case of the cylindrical annulus by Azouni *et al.* (1986) and of convection in a spherical shell by Cordero and Busse (1992). For the purpose of an eventual comparison with experimental observation the computations reported in this paper should be repeated for the case of no-slip boundaries with  $R_e \neq 0$  and  $R_i = 0$ . The computational effort will be more demanding but no significant qualitative changes are expected in that case.

## References

- Ardes, M., Busse, F.H., and Wicht, J., Thermal Convection in Rotating Spherical Shells, *Phys. Earth Plan. Int.* **99**, 55-67, 1997
- Azouni, A., Bolton, E.W., and Busse, F.H., Experimental study of convection

- in a rotating cylindrical annulus, *Geophys. Astrophys. Fluid Dyn.*, **34**, 301-317, 1986
- Busse, F.H.: Thermal instabilities in rapidly rotating systems. *J. Fluid Mech.*, **44**, 441-460, 1970
- Busse, F.H., A simple model of convection in the Jovian atmosphere, *Icarus* **20**, 255-260, 1976
- Busse, F.H., Convection driven zonal flows and vortices in the major planets, *CHAOS*, **4**, 123-134, 1994
- Busse, F.H., Convection flows in rapidly rotating spheres and their dynamo action, *Phys. Fluids*, **14**, 1301-1314, 2002
- Busse, F.H., Carrigan, C.R., Laboratory simulation of thermal convection in rotating planets and stars, *SCIENCE*, **191**, 81-83, 1976
- Busse, F.H., Grote, E., Tilgner, A., On convection driven dynamos in rotating spherical shells. *Studia geoph. et geod.*, **42**, 211-223, 1998
- Christensen, U.R. *et al.*, A numerical dynamo benchmark. *Phys. Earth Plan. Int.*, **128**, 25-34, 2001
- Cordero, S., and Busse, F.H., Experiments on convection in rotating hemispherical shells: Transition to a quasi-periodic state, *Geophys. Res. Letts.*, **19**, 733-736, 1992
- Grote, E., and Busse, F.H., Dynamics of Convection and Dynamos in Rotating Spherical Fluid Shells, *Fluid Dyn. Res.*, **28**, 349-368, 2001
- Hart, J.E., Glatzmaier, G.A., Toomre, J., Space-laboratory and numerical simulations of thermal convection in a rotating hemi-spherical shell with radial gravity, *J. Fluid Mech.*, **173**, 519-544, 1986
- Jones, C.A., Soward, A.M., and Mussa, A.I., The onset of thermal convection in a rapidly rotating sphere, *J. Fluid Mech.*, **405**, 157-179, 2000
- Pino, D., Mercader, I., and Net, M., Thermal and inertial mode of convection in a rapidly rotating annulus, *Phys. Rev. E*, **61**, 1507-1517, 2000
- Rosenzweig, R.E., Browaeys, J., Bacri, J.-C., Zebib, A., and Perzynski, R., Laboratory study of Spherical Convection in Simulated Central Gravity, *Phys. Rev. Letts.*, **83**, 4904-4907, 1997
- Tilgner, A., and Busse, F.H., Finite amplitude convection in rotating spherical fluid shells, *J. Fluid Mech.*, **332**, 359-376, 1997
- Yano, J.-I., Asymptotic theory of thermal convection in rapidly rotating systems, *J. Fluid Mech.*, **243**, 103-131, 1992

- Zhang, K., Vacillating convection in a rotating spherical fluid shell at infinite Prandtl number, *J. Fluid Mech.*, **228**, 607-628, 1991
- Zhang, K., Spiraling columnar convection in rapidly rotating spherical fluid shells, *J. Fluid Mech.*, **236**, 535-556, 1992
- Zhang, K., On coupling between the Poincaré equation and the heat equation, *J. Fluid Mech.*, **268**, 211-229, 1994
- Zhang, K., On coupling between the Poincaré equation and the heat equation: no-slip boundary condition, *J. Fluid Mech.*, **284**, 239-256, 1995
- Zhang, K., and Busse, F.H., On the onset of convection in rotating spherical shells, *Geophys. Astrophys. Fluid Dyn.*, **39**, 119-147, 1987
- Zhang, K., and Busse, F.H., Some recent developments in the theory of convection in rotating systems, in “Nonlinear Instability, Chaos and Turbulence”, Vol 1, L. Debnath and D.N. Riahi, eds., *Computational Mechanics Publications*, WIT Press, 17-69, 1998